

# Efficient Electrochemical Water Splitting with PdSn<sub>4</sub> Dirac Nodal Arc Semimetal

Danil W. Boukhvalov, Chia-Nung Kuo, Silvia Nappini,\* Andrea Marchionni, Gianluca D'Olimpio, Jonathan Filippi, Silvia Mauri, Piero Torelli, Chin Shan Lue, Francesco Vizza, and Antonio Politano\*



Cite This: *ACS Catal.* 2021, 11, 7311–7318



Read Online

ACCESS |



Metrics & More



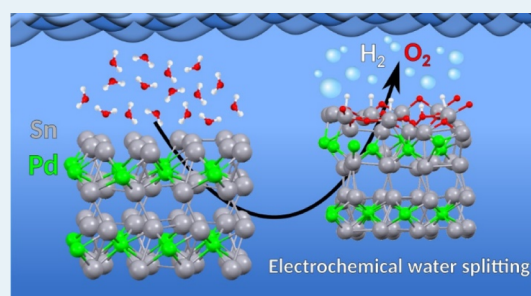
Article Recommendations



Supporting Information

**ABSTRACT:** Recently, several researchers have claimed the existence of superior catalytic activity associated with topological materials belonging to the class of Dirac/Weyl semimetals, owing to the high electron conductivity and charge carrier mobility in these topological materials. By means of X-ray photoelectron spectroscopy, electrocatalytic tests, and density functional theory, we have investigated the chemical reactivity (chemisorption of ambient gases), ambient stability, and catalytic properties of PdSn<sub>4</sub>, a topological semimetal showing Dirac node arcs. We find a Tafel slope of 83 mV in the hydrogen evolution reaction (HER) dec<sup>-1</sup> with an overpotential of 50 mV, with performances resembling those of pure Pd, regardless of its limited amount in the alloy, with a subsequent reduction in the cost of raw materials by ~80%. Remarkably, the PdSn<sub>4</sub>-based electrode shows superior robustness to CO compared to pure Pd and Pt and high stability in water media, although the PdSn<sub>4</sub> surface is prone to oxidation with the formation of a sub-nanometric SnO<sub>2</sub> skin. Moreover, we also assessed the significance of the role of topological electronic states in the observed catalytic properties. Actually, the peculiar atomic structure of oxidized PdSn<sub>4</sub> enables the migration of hydrogen atoms through the Sn–O layer with a barrier comparable with the energy cost of the Heyrovsky step of HER over Pt(111) in acidic media (0.1 eV). On the other hand, the topological properties play a minor role, if existing, contrarily to the recent reports overestimating their contribution in catalytic properties.

**KEYWORDS:** topological materials, hydrogen evolution reaction, electrochemistry, surface science, density functional theory



## INTRODUCTION

Palladium stannide (PdSn<sub>4</sub>) has recently attracted the interest of the scientific community for the evidence of extremely large magnetoresistance and topological electronic states, namely, Dirac arc nodes.<sup>1,2</sup> Among the various possible applications of topological materials,<sup>3–8</sup> topological catalysis has recently emerged as one of the most promising new pathways in electrochemistry<sup>3,4,9–12</sup> since topological electronic states can favor charge transfer between the substrate and the adsorbed chemical species, in order to alter the substrate–adsorbate chemical bond.<sup>13</sup> In several catalytic reactions, the fast transport of electrons from the electrode to the electrolyte is also crucial, such that electrical conductivity and charge carrier mobility are highly desired.<sup>11</sup> Opportunely, most topological materials display high values of electrical conductivity and charge carrier mobility.<sup>14,15</sup> Specifically, Weyl semimetals TaP, NbP, TaAs, and NbAs were shown to be efficient in hydrogen evolution reaction (HER) catalysis, owing to the combination of topological surface states and large room-temperature carrier mobility, associated with bulk Weyl fermions.<sup>10</sup> However, Pt-based topological materials represent more suitable candidates for catalysis, considering that Pt is the state-of-the-art electrode for HER,<sup>16</sup> that is, the cathodic reaction in electrochemical

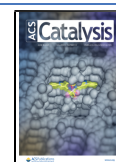
water splitting (HER, 2H<sup>+</sup> → 2H<sub>2</sub> in acidic media or 2H<sub>2</sub>O → 2H<sub>2</sub> + O<sub>2</sub> in alkali media) enabling the production of ultrapure H<sub>2</sub>. Massless chiral fermions associated with large topological charge and Fermi arc surface states in PtAl and PtGa chiral crystals show turnover frequencies (TOFs) as high as 5.6 and 17.1 H<sub>2</sub> s<sup>-1</sup> and overpotentials as low as 14 and 13 mV, respectively, at a current density of 10 mA cm<sup>-2</sup>.<sup>17</sup> Moreover, the Dirac nodal arc semimetal PtSn<sub>4</sub> was found to exhibit a TOF of 1.5 H<sub>2</sub> s<sup>-1</sup> for each active site of PtSn<sub>4</sub> at 100 mV. The linear band crossing in this semimetal provides large room-temperature carrier mobility and conductivity, which can be attributed to the high Fermi velocity of massless Dirac states.<sup>18</sup> This facilitates the rapid charger transfer in the catalysis process and thereby increases the HER kinetics.

On the other hand, the origin of topological surface states, such as Fermi arcs in the materials with covalent (NbAs,<sup>9</sup>

Received: April 11, 2021

Revised: May 16, 2021

Published: June 7, 2021



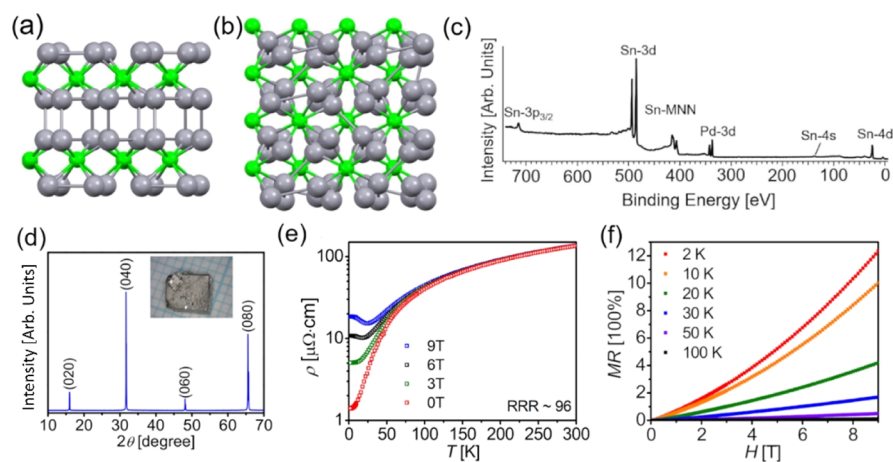


**Figure 1.** (a) Side and (b) top views of the atomic structure of PdSn<sub>4</sub>. (c) Survey XPS spectrum on the as-cleaved PdSn<sub>4</sub> surface. (d) Single-crystal XRD pattern of the samples. Only (0*l*0) peaks can be observed. A photograph of one of the grown single crystals is shown in the inset. (e) Temperature dependence of longitudinal resistivity under different magnetic fields *H* along the *b*-axis. (f) MR with the field applied along the *b*-axis at several temperatures.

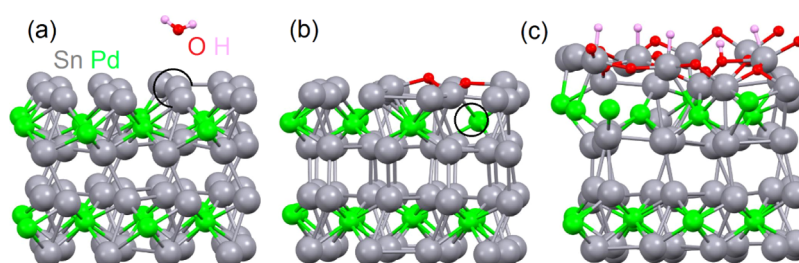


**Figure 2.** Optimized atomic structure of (a) physisorption of one water molecule over the PdSn<sub>4</sub> surface with Sn vacancy sites (PdSn<sub>3.88</sub>) in the surface layer; (b) decomposition of the oxygen molecule over one Pd vacancy (Pd<sub>0.88</sub>Sn<sub>4</sub>) in the subsurface layer, and (c) partial hydrogenation of the oxidized Sn-terminated surface of defect-free PdSn<sub>4</sub>. Vacancies are highlighted by circles.

TaAs,<sup>9</sup> ZrSiS,<sup>19</sup> ZrSiSe,<sup>19</sup> etc.) or metallic (PtSn<sub>4</sub><sup>11,20,21</sup> and PtAl<sup>17</sup>) interlayer bonds is related to the breaking of these bonds at the surface layer upon the formation of the surface. Actually, such broken bonds represent the source of chemical instability of these materials. Correspondingly, oxidation of the surface of topological materials with covalent and metallic interlayer bonds is reported in several recent works.<sup>9,19–21</sup> Thus, possible oxidation of the surface should be considered in the assessment of the catalytic properties of topological materials and the related influence of topologically nontrivial states.

Here, we take the topological Dirac node arc semimetal PdSn<sub>4</sub> as a model system to investigate the relationship between surface chemical reactivity and catalysis. By means of surface-science spectroscopies, density functional theory (DFT), and electrochemical tests, we ruled out previous interpretations regarding the influence of topological features in electronic structure and catalytic activity by demonstrating the pivotal role of the formation of oxide skins on the surface in the catalytic performance.

## RESULTS AND DISCUSSION

PdSn<sub>4</sub> belongs to the *Ccce* [no. 68] space group, and its atomic structure has alternated Pd and Sn layers with a Sn-terminated surface (Figure 1a,b). Although most Sn-based alloys show O contamination in their bulk crystals,<sup>22</sup> the survey spectra taken with X-ray photoelectron spectroscopy (XPS) (Figure 1c) demonstrate the absence of contamination in bulk crystals, which are oriented along a preferential (020) cleavage plan, as

evidenced by the room-temperature X-ray diffraction (XRD) pattern (Figure 1d). The lattice constants evaluated from XRD are  $a = 6.442 \pm 0.002 \text{ \AA}$ ,  $b = 11.445 \pm 0.002 \text{ \AA}$ , and  $c = 6.389 \pm 0.002 \text{ \AA}$ , consistently with previous reports in the literature.<sup>2,23</sup> The single-crystal XRD pattern (Figure 1d) demonstrates that the basal plane of a cleaved crystal is perpendicular to the *b*-axis.

Figure 1e shows the temperature dependence of the electrical resistivity  $\rho(T)$  for the current along the *ac* plane under different magnetic fields. The zero-field resistivity exhibits a clear metallic behavior with the residual resistivity ratio [RRR =  $\rho(300 \text{ K})/\rho(2 \text{ K})$ ]  $\sim 96$ , similar to previous reports.<sup>2</sup> With increasing magnetic field, the resistivity shows a large enhancement and the plateau feature increases distinctly below 25 K. Figure 1f shows the magnetoresistance (MR), defined as  $[\rho(H) - \rho(H = 0)]/\rho(H = 0)$ , for different values of temperature. At each temperature, MR shows no tendency toward saturation in the high-field region. The highest MR approaches 1200% at 2 K and 9 T.

To evaluate the chemical stability of PdSn<sub>4</sub> surface, we modeled physisorption and further decomposition of molecular oxygen and water on defect-free and defective surfaces of PdSn<sub>4</sub>. For defective PdSn<sub>4</sub> surfaces, we considered Sn vacancies in the surface layer and Pd vacancies in the subsurface layer (Figure 2a,b, respectively). These configurations correspond with formulas PdSn<sub>3.88</sub> and Pd<sub>0.88</sub>Sn<sub>4</sub>, respectively.

Two different surface terminations are feasible for (010)-oriented PdSn<sub>4</sub> surfaces with an outermost atomic layer of (i)

Sn (Figure 2a,b) or (ii) Pd (Figure S1 in the Supporting Information). However, the Sn termination is estimated to be more energetically favorable by  $\sim 500$  kJ per surface formula unit. Thus, we have excluded the Pd-terminated configuration from further consideration.

Calculations (Table 1) indicate that, at room temperature, water and carbon monoxide are stably physisorbed only on the

**Table 1. Differential Enthalpy for Physisorption  $\Delta H_{\text{ads}}$ , Differential Gibbs Free Energy at Room Temperature for Physisorption  $\Delta G$ , and, Moreover, Differential Enthalpy of Decomposition  $\Delta H_{\text{dec}}$  (All in kJ/mol) of Selected Molecules over (i) the Defect-Free Surface of PdSn<sub>4</sub> and in Vicinity of (ii) One Sn Vacancy (PdSn<sub>3.88</sub>) in the Surface Layer (Figure 2b) and (iii) One Pd Vacancy (Pd<sub>0.88</sub>Sn<sub>4</sub>) in the Subsurface Layer (Figure 2a)<sup>a</sup>**

substrate	molecule	physisorption		decomposition
		$\Delta H_{\text{ads}}$ [kJ/mol]	$\Delta G$ [kJ/mol]	$\Delta H_{\text{dec}}$ [kJ/mol]
PdSn <sub>4</sub>	O <sub>2</sub>	-63.3	-55.0	-334.5 (-239.7)
	H <sub>2</sub> O	-29.9	+1.4	+82.0
	CO	-13.4	+5.9	
PdSn <sub>3.88</sub>	O <sub>2</sub>	-54.1	-42.8	-352.4 (-300.9)
	H <sub>2</sub> O	-40.2	-8.9	+58.3
	CO	-82.4	-71.1	+428.2
Pd <sub>0.88</sub> Sn <sub>4</sub>	O <sub>2</sub>	-54.7	-43.4	-327.9 (-252.2)
	H <sub>2</sub> O	+30.6	+1.9	+34.8
	CO	-7.5	+11.8	

<sup>a</sup>The numbers in parenthesis correspond to the differential enthalpy (in kJ/mol) of total oxidation of the surface (Figure 2c). Decomposition of CO on PdSn<sub>4</sub> and Pd<sub>0.88</sub>Sn<sub>4</sub> is not considered due to the availability of open Pd sites.

Sn vacancy sites of PdSn<sub>3.88</sub>, while their adsorption is energetically unfavorable on both Pd<sub>0.88</sub>Sn<sub>4</sub> and PdSn<sub>4</sub> surfaces. Further decomposition of water and carbon monoxide at Sn vacancies is energetically unfavorable, although the energy cost of water decomposition on PdSn<sub>3.875</sub> is rather moderate (+58.3 kJ/mol), so that it could be overcome by heating at a temperature less than 100 °C. By contrast, adsorption and decomposition of molecular oxygen is energetically favorable on both defect-free and defective PdSn<sub>4</sub> surfaces.

After decomposition of the first oxygen molecule, subsequent surface oxidation of the whole surface is favored, with differential enthalpy of formation ranging between -239.7 kJ/mol for defect-free PdSn<sub>4</sub> and -300.9 kJ/mol for PdSn<sub>3.88</sub>. Considering the rather large magnitude of the enthalpies of formation and the similarity of the values for different initial atomic structures of the surface, we can propose that all available sites on the surface are unavoidably oxidized.

Specifically, the chemical instability of the PdSn<sub>4</sub> surface is related to the presence of dangling bonds in the formation of the surface upon cleavage. As a matter of fact, contrarily to the case of van der Waals materials (few-layer graphene, h-BN, MoS<sub>2</sub>, etc.), in PdSn<sub>4</sub>, Sn-Pd-Sn layers are connected via metallic Sn-Sn bonds (see Figure 1a,b), whose breaking implies the emergence of electronic states around the Fermi level associated with dangling bonds, which disappear upon surface oxidation (see Figure S2a,b). While the formation of the surface does not provide visible changes in Löwdin charges (only 0.01 e<sup>-</sup>), surface oxidation implies a decrease of charge at the Sn surface sites at 0.7–0.9 e<sup>-</sup>, with an increase of charge

at the Pd sites in the subsurface layer at  $\sim 1.6$  e<sup>-</sup>. This charge redistribution corresponds to the saturation of dangling bonds on the surface. On the other hand, the metallic bond between the 4d states of Pd in the subsurface layer and the 5p states of Sn in the oxide skin still influences the electronic structure of the surface and it prevents the occurrence of a metal–semiconductor transition upon oxidation (see Figure S2c).

Notably, CO adsorption and decomposition is unfavorable on PdSn<sub>4</sub>. On the other hand, CO adsorption on Sn vacancies in PdSn<sub>3.88</sub> is energetically favorable, although it only provides passivation of defects without further formation of carbide-like phases, as instead occurs in the case of CO poisoning of metallic catalysts.<sup>24,25</sup> Thus, we can consider both defect-free and defective PdSn<sub>4</sub> as a material with superior robustness to CO poisoning compared to state-of-the-art metallic catalysts, such as pure Pt and Pd,<sup>25,26</sup> and with good stability in water media, with evident advantages for catalytic applications. Such conclusion is corroborated by vibrational data in Section S7 of the Supporting Information reporting no trace of CO poisoning on PdSn<sub>4</sub> surfaces, contrarily to the case of transition-metal catalysts.

The theoretical model was also validated by experiments on the surface chemical composition and reactivity of PdSn<sub>4</sub> by XPS exploiting the high resolution, tunable photon energy, and fast data acquisition of synchrotron radiation. Pd 3d and Sn 3d core levels were measured for the as-cleaved surface and after exposure to 100 L of CO and  $5 \times 10^5$  L of O<sub>2</sub> (1 L =  $10^{-6}$  Torr-s), as well as after storage in air for 1 and 30 min, as shown in Figure 3a,b. Specifically, the Pd 3d core level (Figure

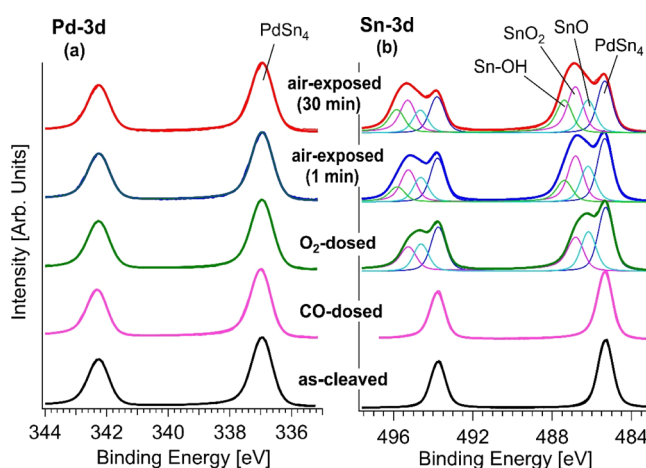


**Figure 3.** Pd 3d (a) and Sn 3d (b) core levels for as-cleaved PdSn<sub>4</sub> and after exposure to CO (100 L), O<sub>2</sub> ( $5 \times 10^5$  L), and air for 1 and 30 min. The photon energy is 800 eV, and the spectra are normalized to the maximum.

3a) of as-cleaved PdSn<sub>4</sub> consists of a doublet at binding energies (BE) of 336.9 (3d<sub>5/2</sub>) and 342.2 (3d<sub>3/2</sub>) eV, corresponding to Pd–Sn bonds.<sup>27–29</sup> No change in Pd 3d spectra was detected upon exposure to CO (100 L), O<sub>2</sub> ( $5 \times 10^5$  L), and air (up to 30 min) at room temperature. Conversely, the Sn 3d doublet, which is set at 485.2 (3d<sub>5/2</sub>) and 493.7 eV (3d<sub>3/2</sub>) for the as-cleaved surface,<sup>27–29</sup> shows evident changes upon exposure to O<sub>2</sub> and air, while no significant modifications were detected after CO dosage (Figure 3b), demonstrating a good tolerance toward CO poisoning.

Selective oxidation of Sn sites observed by XPS suggests that the PdSn<sub>4</sub> surface is terminated by Sn atoms, consistently with our theoretical predictions, with decomposition of O<sub>2</sub> molecules exclusively occurring on Sn sites.

Specifically, two new Sn 3d<sub>5/2</sub> doublets at BEs of 486.2 and 486.8 eV appear upon exposure to O<sub>2</sub>, which can be associated with the formation of SnO (25% of the total spectral area) and SnO<sub>2</sub> (24% of the total spectral area) species, respectively.<sup>28,30</sup> Congruently, the analysis of the O 1s core level (Figure S3) confirms the formation of Sn oxides (SnO and SnO<sub>2</sub>), as suggested by the appearance of a main component (75% of the total spectral area) at ~530.6 eV.<sup>20,30</sup> Two minor components at 532.4 and 533.1 eV appear, ascribed to physisorbed C–O or C–OH species (10% of the total spectral area) and physisorbed H<sub>2</sub>O (15% of the total spectral area), respectively.

The exposure to air induces further modifications of the surface with the emergence of a new Sn 3d<sub>5/2</sub> doublet at 487.3 eV, which can be associated with Sn–OH species<sup>29,30</sup> (Figure 3b). Despite that the water decomposition on defective PdSn<sub>4</sub> is rather moderate (+58.3 kJ/mol), the appearance of Sn–OH groups suggests that water splitting can occur on the air-exposed surface. The decomposition of physisorbed H<sub>2</sub>O and the consequent formation of Sn–OH species can take place on the reactive dangling bonds formed on the PdSn<sub>4</sub> surface upon cleavage or, most likely, on the oxidized region (SnO and SnO<sub>2</sub>) promptly produced upon contact with the oxygen present in ambient atmosphere. Specifically, PdSn<sub>4</sub> forms tin oxide species after only 1 min in air, as shown by the appearance of SnO (19% of the total spectral area), SnO<sub>2</sub> (25% of the total spectral area), and Sn–OH (12% of the total spectral area) species in Figure 3b. Correspondingly, the O 1s spectrum (Figure S3) shows the formation of Sn oxides and Sn–OH bonds, as suggested by the increase of the component at 532.4 eV,<sup>30</sup> as a result of water splitting on the oxidized surface. Physisorbed H<sub>2</sub>O at 534.1 eV is also visible in the O 1s spectrum with a contribution of about 8% of the total spectral area, and the intensity decreases upon a longer storage in air (30 min), while Sn–OH contribution increases. The longer exposure to ambient atmosphere does not change significantly the tin oxide composition (the intensity of SnO and SnO<sub>2</sub> components in Sn 3d remains almost unchanged at 18 and 27% of the total spectral area, respectively), while the increase of Sn–OH species (up to 19%) is accompanied by the simultaneous decrease of PdSn<sub>4</sub> contribution to 28%.

Using quantitative XPS<sup>31–33</sup> (see Section S4 for further information), we estimated the thickness of the SnO<sub>2</sub> skin to be 0.9 ± 0.1 nm already after 1 min in air. After prolonged exposure to air, the thickness of the oxide layer just reaches 1.0 ± 0.1 nm. Thus, passivation is practically achieved nearly instantaneously upon air exposure. This assertion is supported by inspecting the value of thickness upon O<sub>2</sub> exposure in vacuum (the same conditions of green spectra in Figure 3), for which the oxide thickness is already 0.8 ± 0.1 nm.

Based on the results achieved on surface chemical reactivity, we assessed the suitability of PdSn<sub>4</sub> for catalysis, specifically for HER and oxygen evolution reaction (OER).

In the case of HER in acidic media, Pd-deficient PdSn<sub>4</sub> displays an energy cost of the reaction comparable to platinum surfaces (−0.34, 0.21, and −0.10 eV/H<sup>+</sup> for non-oxidized Pd<sub>0.88</sub>Sn<sub>4</sub>, oxidized Pd<sub>0.88</sub>Sn<sub>4</sub>, and pure Pt, respectively, see Figure 4a). Note that hydrogenation of non-oxidized surfaces and oxidized defect-free surface corresponds to the relatively large magnitudes of the negative differential enthalpy of

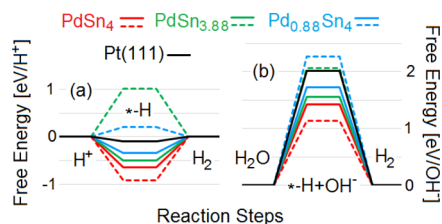


**Figure 4.** Free energy diagrams of HER in (a) acidic and (b) alkali media over various kinds of PdSn<sub>4</sub> surfaces, that is, defect-free and defective surfaces. Solid and dashed lines denote results for pristine and oxidized surfaces, respectively.

formation (−0.5–1 eV//H<sup>+</sup>), which corresponds with almost irreversible hydrogenation of these surfaces. This robust tendency to hydrogenation also corresponds to the unfavorability of the penetration of hydrogen atoms in the subsurface area in contrast to the case of Pd surfaces.<sup>34–36</sup>

On the other hand, these energy gains from hydrogenation partially compensate the energy cost of water splitting in the case of HER in alkali media, thus making the energy cost of this process smaller than for metallic platinum (Figure 4b). This favorability of hydrogenation of defect-free PdSn<sub>4</sub> surfaces makes the Heyrovsky step of HER (\*H + H<sup>+</sup> → H<sub>2</sub>) energetically costly (about 0.7–1 eV/H<sub>2</sub>). Note that in contrast to acidic (H<sup>+</sup>-rich) media, in alkali media, no supply of free hydrogen protons is available. Consequently, the production of molecular hydrogen can be realized only via the Volmer step, corresponding to the recombination of two hydrogen atoms adsorbed on the substrate (2\*H → H<sub>2</sub>). Usually, this step is excluded from consideration, considering the abundance of H<sup>+</sup> in acidic media and the large value of migration barrier (above 1 eV as in the case of non-oxidized PdSn<sub>4</sub>). However, the peculiar atomic structure of oxidized PdSn<sub>4</sub> enables the migration of hydrogen atoms through the Sn–O layer with rather low barriers (0.16–0.22 eV for different concentrations of hydrogen on oxidized surface). The magnitude of this barrier is comparable with the energy cost of the Heyrovsky step of HER over Pt(111) and Pd(111) in acidic media (−0.10 and −0.15 eV, respectively). The origin of this significant decrease of the migration barrier is the spontaneous barrierless migration of hydrogen atoms adsorbed on Sn surface atoms toward O adsorption sites with bridge coordination (Figure 2c), with a subsequent decrease in the distance between two hydrogen atoms to the values about 0.18 nm. This combination of short migration pathway and doping of the SnO layer from the palladium subsurface layer caused by the increase of Löwdin charges at Pd atoms in the subsurface layer leads to decrease of the energy cost of the Volmer step of HER.

When considering reaction kinetics, it is important to note that the Heyrovsky step of HER requires the presence of H<sup>+</sup>(aq) in close vicinity of the hydrogen atom adsorbed on the substrate, contrarily to the Tafel step, which instead requires the presence of a second hydrogen atom adsorbed in over-surface sites. In the case of oxidized (010) surface of PdSn<sub>4</sub>, the areal density of sites suitable for hydrogen adsorption is rather high (see Figure 2c), with a beneficial effect for the Tafel step.

On the other hand, our calculations demonstrate the unsuitability of both oxidized and non-oxidized PdSn<sub>4</sub> for OER due to the large negative (more than 2.00 eV) energy costs of the second or third step (see Figure 5). This large energy cost corresponds to the strong tendency to oxidation of

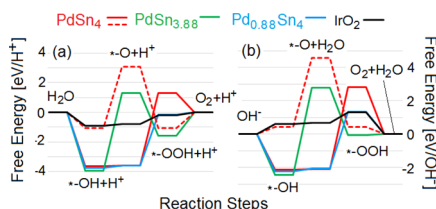


**Figure 5.** Free energy diagrams of OER in acidic (a) and alkali (b) media over various kinds of PdSn<sub>4</sub> surfaces. Oxidized surfaces are depicted by dashed lines.

the Sn-terminated surface of PdSn<sub>4</sub> with the formation of both SnO<sub>x</sub> and Sn(OH)<sub>x</sub> phases, as observed in XPS experiments (Figure 3b). Thus, we rule out the possibility to use PdSn<sub>4</sub> as a catalyst for any reaction involving adsorption of oxygen as the intermediate step.

Theoretical results were validated by direct electrocatalytic tests. The electrocatalytic activity toward HER and OER reactions was investigated by cyclic voltammetry (CV) in 0.1 M HClO<sub>4</sub>.

The electrocatalytic behavior of PdSn<sub>4</sub> reminds more Pd than Sn polycrystalline foils, as clearly shown by the CV curves shown in Figure 6a. Indeed, the HER and OER onset potentials are ca. −0.05 and 1.70 V, respectively. Furthermore, the general shape of the CV curve is more similar to Pd than to Sn.

Interestingly, the HER performance improves whenever the PdSn<sub>4</sub> surface is exposed to higher potentials (Figure 6c). Indeed, if we consider the current density at −0.10 V versus

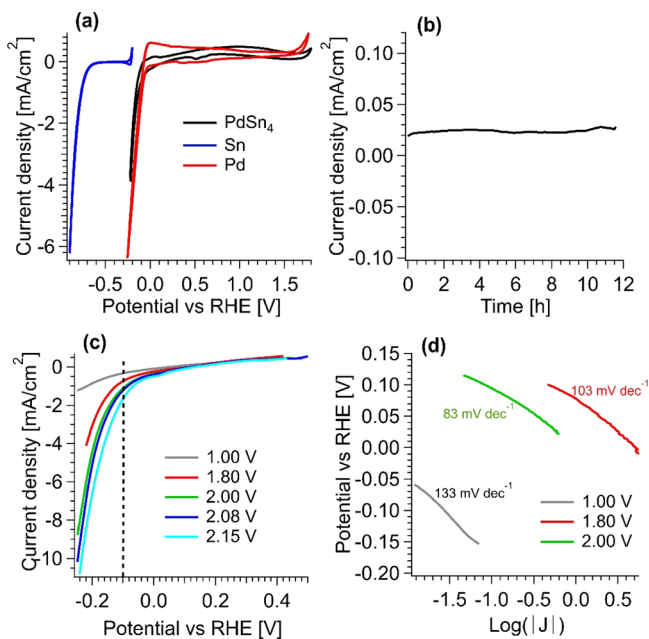


**Figure 6.** (a) CVs of Sn (blue curve), Pd (red curve), and PdSn<sub>4</sub> (black curve) foils in 0.1 M HClO<sub>4</sub>, measured with a scan rate of 20 mV s<sup>−1</sup>. (b) Chronoamperometric curve of PdSn<sub>4</sub> during HER in 0.1 M HClO<sub>4</sub> at a potential of −0.15 V vs RHE. (c) Current densities of PdSn<sub>4</sub> measured in the HER region cycled at different upper inversion potentials: 1.00 V (gray curve), 1.80 V (red curve), 2.00 V (green curve), 2.08 V (dark blue curve), and 2.15 V (light blue curve). (d) Tafel plots with the corresponding slopes of PdSn<sub>4</sub> treated at different potentials before testing HER in 0.1 M HClO<sub>4</sub>: 1.00 V (gray curve), 1.8 V (red curve), and 2.00 V (green curve).

RHE, the absolute value of cathodic current increases from 0.22 to 1.77 mA cm<sup>−2</sup> when the electrode was exposed to potential from 1.00 to 2.15 V versus RHE, respectively. Correspondingly, Tafel slopes were estimated to be 133, 103, and 83 mV dec<sup>−1</sup> after a treatment at potentials of 1.00, 1.80, and 2.00 V versus RHE, respectively (Figure 6d). However, for exposure potential higher than 1.80 V versus RHE, the CVs showed a cathodic peak at ca. 0.5 V versus RHE during the backward scan (Figure 6a), consistently with the reduction of palladium oxide.<sup>37</sup> Furthermore, it is well known that potentials over 1.40 V versus RHE can produce multilayered palladium oxide on Pd foils,<sup>38</sup> which could explain the structured peak for potentials over 2.00 V versus RHE.

To assess the electrochemical stability of PdSn<sub>4</sub> in HER conditions, we measured the chronoamperometric curve (Figure 6b) at an applied potential of −0.15 V versus RHE on an electrode previously treated up to 2.20 V versus RHE, finding long-term current stability in a timescale extended up to 12 h.

The OER performances of PdSn<sub>4</sub> in 0.1 M HClO<sub>4</sub> exhibited an onset potential near 1.70 V versus RHE, close to its value for pure Pd (Figure 6a), consistently with theoretical predictions in Figure 5. Congruently, also the Tafel slope of PdSn<sub>4</sub> (387 mV dec<sup>−1</sup>) was estimated from the Tafel plot (Figure S5), showing a value similar to that of pure Pd (205 mV dec<sup>−1</sup>).

To examine in depth the stability of PdSn<sub>4</sub>, CVs (5000 cycles) were performed as accelerated aging tests between two potential windows: (i) −0.1 and 1.0 V and (ii) −0.1 and 2.2 V versus RHE (see Section S10 and Figure S10 in the Supporting Information). The first experiment up to 1.0 V exhibited a decreased activity after some cycles and then the performance remained quite stable. In the second test, CV up to 2.2 V showed that the HER activity drastically decreased in a few tens of cycles, indicating that the performance of the catalyst is negatively affected by a prolonged activity up to a high potential, such as 2.2 V. The scanning electron microscopy characterization (see Figures S11 and S12 in the Supporting Information), conducted before and after the aging tests, displayed a negligible morphological modification after the first experiment (up to 1.0 V), while a dramatic modification was observed after the second one (up to 2.2 V). In both cases, the major visible alterations are probably due to the exfoliation of less dense materials, such as hydroxides or oxides, formed on the surface upon contact with the electrolyte. In order to confirm this hypothesis, the surface composition of PdSn<sub>4</sub> was studied ex situ by XPS after 30 min of storage in the electrolyte and after several voltammetry cycles up to a potential of 2.2 V versus RHE (see Section S10 and Figures S13 and S14 in the Supporting Information). The high surface sensitivity of the XPS technique evidenced the formation of both tin oxide and palladium oxide species, as well as the formation of metallic Pd sites after aging cycles up to 2.2 V.

The irreversible formation of metallic Pd sites and surface oxidation can strongly affect the catalytic activity of PdSn<sub>4</sub>, evidencing the key contribution of the surface modification induced by the catalytic conditions. The great similarity of the CV profile of PdSn<sub>4</sub> with that of pure Pd (Figure 6a) suggests that Pd surface sites could have a key role as active catalytic sites in the electrochemical performance of PdSn<sub>4</sub> catalyst.

Finally, to assess the impact of topological states on the electrochemical behavior of PdSn<sub>4</sub>, we also tested the material with Fe-phthalocyanines deposited onto the electrode surface

(Section S11 in the Supporting Information). The obtained results further confirm that the absence of effects related to the topological states of PdSn<sub>4</sub>, removed by magnetic impurities (Fe centers), on its electrocatalytic activity.

To extend the validity of our model also to parental compounds, we performed a surface-science, catalytic, and theoretical investigation on PtSn<sub>4</sub>, finding similar results, as reported in Section S6 of the Supporting Information. Therefore, we can infer that the physicochemical model here proposed for PdSn<sub>4</sub> is also valid for its parental compounds, such as PtSn<sub>4</sub> and related systems.

## CONCLUSIONS

We assessed the chemical reactivity and the catalytic properties of the PdSn<sub>4</sub> Dirac node arc semimetal. We observed a Tafel slope in the HER of 83 mV dec<sup>-1</sup>, with an overpotential of 50 mV, similar to pure Pd. Thus, the PdSn<sub>4</sub> alloy, in spite of the limited amount of Pd in the alloy, displays practically the same catalytic properties of precious Pd element, with a reduction in the cost of raw materials by ~80%. More interestingly, the PdSn<sub>4</sub>-based electrode shows superior robustness to CO compared to pure Pd and Pt and high stability in water media.

However, a careful surface-science investigation provides evidence that the high efficiency of HER cannot be explained only with the effect of topologically nontrivial electronic states, which however influence fast electron transfer. As a matter of fact, we find that the PdSn<sub>4</sub> surface is prone to oxidation with the formation of a sub-nanometric SnO<sub>2</sub> skin, whose peculiar atomic structure permits the migration of H atoms through the Sn–O layer with a barrier similar to the energy cost of the Heyrovsky step of HER over Pt(111) in acidic media (0.1 eV). A similar picture is also valid for parental compounds, such as PtSn<sub>4</sub>.

Our results indicate the key role of surface processes in catalysis with topological materials, while the current state-of-the-art is overestimating the role of topological states, which instead are relevant for kinetics only.

In addition, our findings suggest the possibly high potential interest of PdSn<sub>4</sub> in electrocatalysis, due to the catalytic performances resembling Pt and Pd but with a reduced loading of precious Pd element, with both economic and environmental advantages.

Finally, we also highlight the differences in the pathways of HER in acidic and alkali media and the crucial role of Volmer step for H<sub>2</sub> production in alkali conditions.

Novel concepts here developed are expected to open new avenues for catalysis in oxidative environments, also considering that they can be applied to other materials with similar physicochemical and structural properties. Moreover, it is evident that the catalytic activity of the surface oxide phase could be easily optimized, although PdSn<sub>4</sub> is already competitive with state-of-the-art materials (pure Pt and Pd) already in the first implementation of the catalytic device.

## METHODS

**Single-Crystal Growth and Characterization of Grown Crystals.** Single crystals of PdSn<sub>4</sub> were grown from the Sn flux in the temperature range selected according to the Pd–Sn binary phase diagram.<sup>40</sup> The starting materials of Pd (99.95%) and Sn (99.99%) with a molar ratio of 1:44 were inserted in an aluminum crucible and sealed into a quartz ampoule under high vacuum. The ampoule was heated at a rate

of 100 °C h<sup>-1</sup> and held at 900 °C for 10 h. After all the materials were homogenized, the ampoule was cooled down to 350 °C at a rate of 50 °C h<sup>-1</sup> and then slowly cooled to 250 °C at a rate of 1 °C h<sup>-1</sup>. The excess Sn flux was removed by spinning the ampoule in the centrifuge. Plate-like PdSn<sub>4</sub> single crystals with sizes about 4 × 4 × 1 mm<sup>3</sup> were obtained, as shown in the inset of Figure 1d. XRD data were taken with Cu Kα radiation at room temperature. Electrical transport measurements up to 9 T were conducted in a Quantum Design PPMS-9 with the conventional four-wire method.

The stability of the crystals in both alkaline and acid environments is ensured by the analysis reported in Section S8 of the Supporting Information.

The thermal stability was assessed in Section S9 of the Supporting Information.

**Computational Methods.** The atomic structure and energetics of various configurations of various gases adsorbed on PdSn<sub>4</sub> were studied by DFT using the QUANTUM ESPRESSO code<sup>9</sup> (version 6.0) and the GGA-PBE approximation with van der Waals (vdW) corrections.<sup>10</sup> Energy cutoffs of 25 and 400 Ry for the plane-wave expansion of the wave functions and the charge density, respectively, and the 5 × 5 × 3 Monkhorst–Pack *k*-point grid for the Brillouin zone sampling<sup>11</sup> were used. To model the PdSn<sub>4</sub> surface, we considered a 2 × 1 × 2 supercell-based slab of 80 atoms (Figure 2).

The values of the enthalpies of physisorption were calculated by the standard formula

$$\Delta H_{\text{phys}} = [E_{\text{host+mol}} - (E_{\text{host}} + E_{\text{mol}})]$$

where  $E_{\text{host}}$  is the total energy of the surface before adsorption and  $E_{\text{mol}}$  is the energy of a single molecule of the considered species in an empty box. In the case of water adsorption, only adsorption in the gaseous phase is considered. The energy of chemical adsorption is defined as the difference between the total energy of the system after and before decomposition of physisorbed molecules on the surface. For the case of physisorption, we also evaluated the differential Gibbs free energy by the formula

$$\Delta G = \Delta H - T\Delta S$$

where  $T$  is the temperature and  $\Delta S$  is the change of entropy of the adsorbed molecule estimated by the change of entropy in the process of gas-to-liquid transition by the standard formula

$$\Delta S = \Delta H_{\text{vaporization}}/T$$

where  $\Delta H_{\text{vaporization}}$  is the measured enthalpy of vaporization. All formulas of reaction steps and technical details for the calculations of the HER and OER are the same as used for the modeling of these reactions over a Pt(111) substrate.<sup>12,13</sup> A value for overpotentials of  $U = 1.23$  and  $0.89$  eV was used for OER in acidic and alkali medium, respectively.

**Synchrotron-Based XPS.** XPS measurements were carried out on the APE-HE beamline at Elettra Sincrotrone in Trieste (Italy). XPS spectra were acquired with an Omicron EA125 hemispherical electron energy analyzer in normal emission configuration using a photon energy of 800 eV with an overall energy resolution of about 0.1 eV.

Pd 3d and Sn 3d core levels were analyzed using Doniach–Sunjić doublet line shapes convoluted with a Gaussian function, and the O 1s core level was decomposed using Voigt line shape functions after the subtraction of a Shirley-type background.

**Electrochemical Tests.** Before the electrochemical characterization, the PdSn<sub>4</sub> foil was embedded in an epoxy resin to facilitate surface polishing and the result reproducibility.

A common three-electrode glass cell was used for the electrochemical tests with a Pt wire as the counter electrode and Ag/AgCl/KCl sat. as the reference electrode. All potentials were referred to the RHE to include the pH effects. Equipment was cleaned with a mixture of water and 2-propanol and rinsed several times with ultrapure water (18.2 MΩ). The electrolyte was a 0.1 M solution of perchloric acid (70%, Sigma-Aldrich) in ultrapure water purged with nitrogen.

The electrochemical experiments were conducted with a Princeton Applied Research PARSTAT 2277 potentiostat. All current measurements were normalized to the geometric surface area of the electrode. CV experiments were conducted at 20 mV s<sup>-1</sup>, while slow linear sweep experiments to obtain the Tafel slope were performed at 1 mV s<sup>-1</sup> between two potential windows: (i) -0.1 and 1.0 V and (ii) -0.1 and 2.2 V versus RHE.

## ■ ASSOCIATED CONTENT

### SI Supporting Information

The Supporting Information is available free of charge at <https://pubs.acs.org/doi/10.1021/acscatal.1c01653>.

Alternative atomic structure of the Pd-terminated PdSn<sub>4</sub> surface, density of states, O 1s core level XPS spectra, determination of the thickness of the oxide skin, experimental OER tests, comparison with PtSn<sub>4</sub>, assessment of the eventual impact of CO poisoning, stability in acidic and alkaline environments, thermal stability, long-term stability of electrocatalytic activity, and effect of Fe doping on electrocatalytic activity (PDF)

## ■ AUTHOR INFORMATION

### Corresponding Authors

**Silvia Nappini** – Consiglio Nazionale delle Ricerche (CNR)-Istituto Officina dei Materiali (IOM), Laboratorio TASC, 34149 Trieste, Italy; [orcid.org/0000-0002-4944-5487](https://orcid.org/0000-0002-4944-5487); Email: [nappini@iom.cnr.it](mailto:nappini@iom.cnr.it)

**Antonio Politano** – INSTM and Department of Physical and Chemical Sciences, University of L'Aquila, 67100 L'Aquila, Abruzzo, Italy; CNR-IMM Istituto per la Microelettronica e Microsistemi, I-95121 Catania, Italy; [orcid.org/0000-0002-4254-2102](https://orcid.org/0000-0002-4254-2102); Email: [antonio.politano@univaq.it](mailto:antonio.politano@univaq.it)

### Authors

**Danil W. Boukhalov** – College of Science, Institute of Materials Physics and Chemistry, Nanjing Forestry University, Nanjing 210037, P. R. China; Theoretical Physics and Applied Mathematics Department, Ural Federal University, 620002 Ekaterinburg, Russia; [orcid.org/0000-0002-2286-3443](https://orcid.org/0000-0002-2286-3443)

**Chia-Nung Kuo** – Department of Physics, National Cheng Kung University, 70101 Tainan, Taiwan

**Andrea Marchionni** – Consiglio Nazionale delle Ricerche (CNR)-Istituto di Chimica dei Composti Organometallici (ICCOM), Area della Ricerca di Firenze, S0019 Sesto Fiorentino, Italy

**Gianluca D'Olimpio** – INSTM and Department of Physical and Chemical Sciences, University of L'Aquila, 67100 L'Aquila, Abruzzo, Italy; [orcid.org/0000-0002-6367-3945](https://orcid.org/0000-0002-6367-3945)

**Jonathan Filippi** – Consiglio Nazionale delle Ricerche (CNR)-Istituto di Chimica dei Composti Organometallici (ICCOM), Area della Ricerca di Firenze, S0019 Sesto Fiorentino, Italy

**Silvia Mauri** – Consiglio Nazionale delle Ricerche (CNR)-Istituto Officina dei Materiali (IOM), Laboratorio TASC, 34149 Trieste, Italy

**Piero Torelli** – Consiglio Nazionale delle Ricerche (CNR)-Istituto Officina dei Materiali (IOM), Laboratorio TASC, 34149 Trieste, Italy; Elettra-Sincrotrone S.C.p.A, 34149 Trieste, Italy

**Chin Shan Lue** – Department of Physics, National Cheng Kung University, 70101 Tainan, Taiwan

**Francesco Vizza** – Consiglio Nazionale delle Ricerche (CNR)-Istituto di Chimica dei Composti Organometallici (ICCOM), Area della Ricerca di Firenze, S0019 Sesto Fiorentino, Italy

Complete contact information is available at:

<https://pubs.acs.org/doi/10.1021/acscatal.1c01653>

## Author Contributions

D.W.B., C.-N.K., and S.N. contributed equally. The project was conceived and coordinated by A.P. XPS experiments were carried out by G.D. and S.M. under the supervision of P.T. with data analysis by G.D. and S.N. Electrochemical tests were performed by A.M. and J.F. under the supervision of F.V. The theoretical model was elaborated by D.W.B. The samples were grown by C.-N.K., C.S.L., and A.P. Transport experiments were carried out by C.-N.K. and C.S.L. The paper was written by D.W.B., S.N., and A.P.

## Notes

The authors declare no competing financial interest.

## ■ ACKNOWLEDGMENTS

D.W.B. acknowledges the support from the Ministry of Science and Higher Education of the Russian Federation (through the basic part of the government mandate, project no. FEUZ-2020-0060 and Jiangsu Innovative and Entrepreneurial Talents Project). A.M., J.F., and F.V. acknowledge the Italian Ministry of University and Research MUR by the PRIN 2017 (no. 2017YH9MRK) and MISE FISR 2019 AMPERE (FISR2019\_01294) projects for the financial support.

## ■ REFERENCES

- (1) Jo, N. H.; Wu, Y.; Wang, L.-L.; Orth, P. P.; Downing, S. S.; Manni, S.; Mou, D.; Johnson, D. D.; Kaminski, A.; Bud'Ko, S. L.; Canfield, P. C. Extremely Large Magnetoresistance and Kohler's Rule in PdSn<sub>4</sub>: A Complete Study of Thermodynamic, Transport, and Band-Structure Properties. *Phys. Rev. B* **2017**, *96*, 165145.
- (2) Xu, C. Q.; Zhou, W.; Sankar, R.; Xing, X. Z.; Shi, Z. X.; Han, Z. D.; Qian, B.; Wang, J. H.; Zhu, Z.; Zhang, J. L.; Bangura, A. F.; Hussey, N. E.; Xu, X. Enhanced Electron Correlations in the Binary Stannide PdSn<sub>4</sub>: A Homologue of the Dirac Nodal Arc Semimetal PtSn<sub>4</sub>. *Phys. Rev. Mater.* **2017**, *1*, 064201.
- (3) Qu, Q.; Liu, B.; Liang, J.; Li, H.; Wang, J.; Pan, D.; Sou, I. K. Expediting Hydrogen Evolution through Topological Surface States on Bi<sub>2</sub>Te<sub>3</sub>. *ACS Catal.* **2020**, *10*, 2656–2666.
- (4) Xu, Q.; Li, G.; Zhang, Y.; Yang, Q.; Sun, Y.; Felser, C. Descriptor for Hydrogen Evolution Catalysts Based on the Bulk Band Structure Effect. *ACS Catal.* **2020**, *10*, 5042–5048.
- (5) Sahni, B.; Vikram; Kangsabanik, J.; Alam, A. Reliable Prediction of New Quantum Materials for Topological and Renewable-Energy Applications: A High-Throughput Screening. *J. Phys. Chem. Lett.* **2020**, *11*, 6364–6372.

- (6) Xu, H.; Zhou, J.; Wang, H.; Li, J. Giant Photonic Response of Mexican-Hat Topological Semiconductors for Mid-Infrared to Terahertz Applications. *J. Phys. Chem. Lett.* **2020**, *11*, 6119–6126.
- (7) Han, F.; Andrejevic, N.; Nguyen, T.; Kozii, V.; Nguyen, Q. T.; Hogan, T.; Ding, Z.; Pablo-Pedro, R.; Parjan, S.; Skinner, B.; Alatas, A.; Alp, E.; Chi, S.; Fernandez-Baca, J.; Huang, S.; Fu, L.; Li, M. Quantized Thermoelectric Hall Effect Induces Giant Power Factor in a Topological Semimetal. *Nat. Commun.* **2020**, *11*, 6167.
- (8) Yan, M.; Lu, J.; Li, F.; Deng, W.; Huang, X.; Ma, J.; Liu, Z. On-Chip Valley Topological Materials for Elastic Wave Manipulation. *Nat. Mater.* **2018**, *17*, 993–998.
- (9) Politano, A.; Chiarello, G.; Li, Z.; Fabio, V.; Wang, L.; Guo, L.; Chen, X.; Boukhvalov, D. W. Toward the Effective Exploitation of Topological Phases of Matter in Catalysis: Chemical Reactions at the Surfaces of NbAs and TaAs Weyl Semimetals. *Adv. Funct. Mater.* **2018**, *28*, 1800511.
- (10) Rajamathi, C. R.; Gupta, U.; Kumar, N.; Yang, H.; Sun, Y.; Süß, V.; Shekhar, C.; Schmidt, M.; Blumtritt, H.; Werner, P.; Yan, B.; Parkin, S.; Felser, C.; Rao, C. N. R. Weyl Semimetals as Hydrogen Evolution Catalysts. *Adv. Mater.* **2017**, *29*, 1606202.
- (11) Li, G.; Fu, C.; Shi, W.; Jiao, L.; Wu, J.; Yang, Q.; Saha, R.; Kamminga, M. E.; Srivastava, A. K.; Liu, E.; Yazdani, A. N.; Kumar, N.; Zhang, J.; Blake, G. R.; Liu, X.; Fahlman, M.; Wirth, S.; Auffermann, G.; Gooth, J.; Parkin, S.; Madhavan, V.; Feng, X.; Sun, Y.; Felser, C. Dirac Nodal Arc Semimetal  $\text{PtSn}_4$ : An Ideal Platform for Understanding Surface Properties and Catalysis for Hydrogen Evolution. *Angew. Chem.* **2019**, *58*, 13107–13112.
- (12) Li, Z.; Wei, B. Topological Materials and Topologically Engineered Materials: Properties, Synthesis, and Applications for Energy Conversion and Storage. *J. Mater. Chem. A* **2020**, *9*, 1297–1313.
- (13) Li, G.; Felser, C. Heterogeneous Catalysis at the Surface of Topological Materials. *Appl. Phys. Lett.* **2020**, *116*, 070501.
- (14) Hu, J.; Xu, S.-Y.; Ni, N.; Mao, Z. Transport of Topological Semimetals. *Annu. Rev. Mater. Res.* **2019**, *49*, 207–252.
- (15) Culcer, D.; Cem Keser, A.; Li, Y.; Tkachov, G. Transport in Two-Dimensional Topological Materials: Recent Developments in Experiment and Theory. *2D Mater.* **2020**, *7*, 022007.
- (16) Zheng, J.; Sheng, W.; Zhuang, Z.; Xu, B.; Yan, Y. Universal Dependence of Hydrogen Oxidation and Evolution Reaction Activity of Platinum-Group Metals on pH and Hydrogen Binding Energy. *Sci. Adv.* **2016**, *2*, No. e1501602.
- (17) Yang, Q.; Li, G.; Manna, K.; Fan, F.; Felser, C.; Sun, Y. Topological Engineering of Pt-Group-Metal-Based Chiral Crystals toward High-Efficiency Hydrogen Evolution Catalysts. *Adv. Mater.* **2020**, *32*, 1908518.
- (18) Wu, Y.; Wang, L.-L.; Mun, E.; Johnson, D. D.; Mou, D.; Huang, L.; Lee, Y.; Bud'ko, S. L.; Canfield, P. C.; Kaminski, A. Dirac Node Arcs in  $\text{PtSn}_4$ . *Nat. Phys.* **2016**, *12*, 667–671.
- (19) Boukhvalov, D. W.; Edla, R.; Cupolillo, A.; Fabio, V.; Sankar, R.; Zhu, Y.; Mao, Z.; Hu, J.; Torelli, P.; Chiarello, G.; Ottaviano, L.; Politano, A. Surface Instability and Chemical Reactivity of  $\text{ZrSiS}$  and  $\text{ZrSiSe}$  Nodal-Line Semimetals. *Adv. Funct. Mater.* **2019**, *29*, 1900438.
- (20) Boukhvalov, D. W.; Marchionni, A.; Filippi, J.; Kuo, C.-N.; Fujii, J.; Edla, R.; Nappini, S.; D'Olimpio, G.; Ottaviano, L.; Lue, C. S.; Torelli, P.; Vizza, F.; Politano, A. Efficient Electrochemical Hydrogen Evolution Reaction with  $\text{PtSn}_4$  Via Surface Oxidation. *J. Mater. Chem. A* **2020**, *8*, 2349–2355.
- (21) D'Olimpio, G.; Boukhvalov, D. W.; Fujii, J.; Torelli, P.; Marchionni, A.; Filippi, J.; Kuo, C.-N.; Edla, R.; Ottaviano, L.; Lue, C. S.; Vizza, F.; Nappini, S.; Politano, A. Catalytic Activity of  $\text{PtSn}_4$ : Insights from Surface-Science Spectroscopies. *Appl. Surf. Sci.* **2020**, *514*, 145925.
- (22) Lamuta, C.; Campi, D.; Pagnotta, L.; Dasadia, A.; Cupolillo, A.; Politano, A. Determination of the Mechanical Properties of  $\text{SnSe}$ , a Novel Layered Semiconductor. *J. Phys. Chem. Solids* **2018**, *116*, 306–312.
- (23) Nylén, J.; Garcia Garcia, F. J.; Mosel, B. D.; Pöttgen, R.; Häussermann, U. Structural Relationships, Phase Stability and Bonding of Compounds  $\text{PdSn}_n$  ( $n = 2, 3, 4$ ). *Solid State Sci.* **2004**, *6*, 147–155.
- (24) Farrell, C. G.; Gardner, C. L.; Ternan, M. Experimental and Modelling Studies of CO Poisoning in Pem Fuel Cells. *J. Power Sources* **2007**, *171*, 282–293.
- (25) Ponrouch, A.; Garbarino, S.; Guay, D. Effect of the Nanostructure on the CO Poisoning Rate of Platinum. *Electrochem. Commun.* **2009**, *11*, 834–837.
- (26) Ren, H.; Humbert, M. P.; Menning, C. A.; Chen, J. G.; Shu, Y.; Singh, U. G.; Cheng, W.-C. Inhibition of Coking and CO Poisoning of Pt Catalysts by the Formation of Au/Pt Bimetallic Surfaces. *Appl. Catal., A* **2010**, *375*, 303–309.
- (27) Marakatti, V. S.; Sarma, S. C.; Sarkar, S.; Krajčí, M.; Gaigneaux, E. M.; Peter, S. C. Synthetically Tuned Pd-Based Intermetallic Compounds and Their Structural Influence on the  $\text{O}_2$  Dissociation in Benzylamine Oxidation. *ACS Appl. Mater. Interfaces* **2019**, *11*, 37602–37616.
- (28) Bai, X.; Chen, W.; Zhao, C.; Li, S.; Song, Y.; Ge, R.; Wei, W.; Sun, Y. Exclusive Formation of Formic Acid from  $\text{CO}_2$  Electroreduction by a Tunable Pd-Sn Alloy. *Angew. Chem.* **2017**, *129*, 12387–12391.
- (29) Wu, P.; Huang, Y.; Kang, L.; Wu, M.; Wang, Y. Multisource Synergistic Electrocatalytic Oxidation Effect of Strongly Coupled PdM ( $M = \text{Sn, Pb}$ )/N-doped Graphene Nanocomposite on Small Organic Molecules. *Sci. Rep.* **2015**, *5*, 14173.
- (30) Jadhav, H.; Suryawanshi, S.; More, M. A.; Sinha, S. Pulsed Laser Deposition of Tin Oxide Thin Films for Field Emission Studies. *Appl. Surf. Sci.* **2017**, *419*, 764–769.
- (31) Alexander, M. R.; Thompson, G. E.; Zhou, X.; Beamson, G.; Fairley, N. Quantification of Oxide Film Thickness at the Surface of Aluminium Using XPS. *Surf. Interface Anal.* **2002**, *34*, 485–489.
- (32) Sciortino, L.; Cicero, U. L.; Magnano, E.; Piš, I.; Barbera, M. Surface investigation and aluminum oxide estimation on test filters for the ATHENA X-IFU and WFI detectors. *Proceedings of SPIE Volume 9905, Space Telescopes and Instrumentation 2016: Ultraviolet to Gamma Ray*, 2016; p 990566. <https://doi.org/10.1117/12.2232376>.
- (33) Walton, J.; Alexander, M. R.; Fairley, N.; Roach, P.; Shard, A. G. Film Thickness Measurement and Contamination Layer Correction for Quantitative XPS. *Surf. Interface Anal.* **2016**, *48*, 164–172.
- (34) Muschiol, U.; Schmidt, P. K.; Christmann, K. Adsorption and Absorption of Hydrogen on a Palladium (210) Surface: A Combined LEIS,  $\Delta\phi$  and HREELS Study. *Surf. Sci.* **1998**, *395*, 182–204.
- (35) Farias, D.; Patting, M.; Rieder, K. H. Helium Diffraction Investigations of the Transition of Chemisorbed Hydrogen into Subsurface Sites on Palladium Surfaces. *Phys. Status Solidi A* **1997**, *159*, 255–262.
- (36) Schilbe, P.; Farias, D.; Rieder, K. H. HREELS Studies of Hydrogen Adsorption on Pd(311). *Surf. Rev. Lett.* **1998**, *5*, 473–478.
- (37) Zhang, A. J.; Gaur, M.; Birss, V. I. Growth of Thin, Hydrous Oxide Films at Pd Electrodes. *J. Electroanal. Chem.* **1995**, *389*, 149–159.
- (38) Hu, C.-C.; Wen, T.-C. Voltammetric Investigation of Palladium Oxides—I: Their Formation/Reduction in NaOH. *Electrochim. Acta* **1995**, *40*, 495–503.
- (39) Cherevko, S.; Zeradjanin, A. R.; Topalov, A. A.; Kulyk, N.; Katsounaros, I.; Mayrhofer, K. J. J. Dissolution of Noble Metals During Oxygen Evolution in Acidic Media. *ChemCatChem* **2014**, *6*, 2219–2223.
- (40) Okamoto, H. Pd-Sn (Palladium-Tin). *J. Phase Equilib. Diffus.* **2012**, *33*, 253–254.